An Investigation on Cooling Performance of Air-Cooled Heat Exchangers Used in Coal Seam Gas Production

Yuanshen Lu, Zhiqiang Guan, Kamel Hooman & Prashant S. Parulekar

Taylor & Francis
Taylor & Francis Group

An Investigation on Cooling Performance of Air-Cooled Heat Exchangers Used in Coal Seam Gas Production

Yuanshen Lu[a,b], Zhiqiang Guan[a,b], Kamel Hooman [a,b], and Prashant S. Parulekar[c]

[a]Queensland Geothermal Energy Centre of Excellence, St. Lucia, Queensland, Australia; [b]School of Mechanical and Mining Engineering, University of Queensland, St. Lucia, Queensland, Australia; [c]Arrow Energy, Brisbane, Queensland, Australia

ABSTRACT

This paper reports an investigation into a practical cooling issue on a type of fan-forced finned-tube heat exchangers used in Queensland's coal seam gas (CSG) industry. CSG compression facilities in some production sites suffered underproduction in recent summers because of frequent automatic engine shutdowns. The problem is not expected by the manufacturer's design. However, it is suspected of being related to the control systems on the compression facilities triggering the overheating-protection shutdowns due to possible deficiencies in one or some water/gas cooling loops in the facilities' air-cooled heat exchangers. Therefore, to understand which heat exchangers and what exact reasons cause the unexpected cooling issue, an investigation has been carried out on the cooler units of the gas compression facilities. A field instrumentation measurement on one operating cooler unit has been done, followed by an analysis using a one-dimensional analytical model and a three-dimensional computational fluid dynamics model. The experimental results are used to validate both the models. Then the cooling performance of the cooler unit under the summer peak condition is predicted by the verified models. The prediction suggests that the water inlet temperature in one particular cooler section is higher than its upper limit defined by the manufacturer, due to poor cooling at high ambient temperatures. The lower cooling performance is caused by large reductions in the cooler air speed and total heat transfer coefficient, which are related to less efficiency of the cooler fans, more airflow resistance, and fouling on both sides of the finned tubes.

Introduction

Fan-forced finned-tube heat exchangers are widely used in air-to-liquid cooling/condensing systems in various industries. In natural gas industries, most cooling demands in gas processing rely on this type of heat exchangers, as circular finned tubes are usually most economical for the requirements such as resistance to high tube-side pressure [1]. Coal seam gas (CSG), mostly composed of methane, is a common type of natural gas and its mining technologies are very mature nowadays. Queensland reserves abundant CSG resource, and after two decades of boom, the CSG industry has become one of the cornerstone economic elements in Queensland [2]. Most CSG produced in Queensland is exported overseas, while the rest is supplied to the local markets. On most CSG production sites, the raw gas extracted from gas wells needs to be dehydrated and compressed before being transported through pressurized pipelines. As the compression process generates large amounts of heat, the air-cooled heat

exchangers are used to reject the redundant heat. Therefore, the performance of the cooling systems in the process is critical to the overall production efficiency. During many years of operations, it is found that the CSG production in many gas sites suffers considerable reductions in summer days. It is suspected that the problem is related to possible degradation in the cooling performance due to the weather conditions in regional Queensland. Therefore, the Queensland Geothermal Energy Centre of Excellence (QGECE) is involved in investigating the exact reasons causing the cooling performance issues on these CSG production lines.

The CSG production facilities that QGECE investigates are a typical type seen in natural gas industry. In a basic unit of these facilities, raw CSG piped from gas production wells undergoes four stages of compressions in a four-cylinder compressor. After each compression stage, the gas is piped to a circular finned-tube heat exchanger, namely, a gas stage cooler (GS), to be cooled down. Once the four stages of compression are complete, most of the
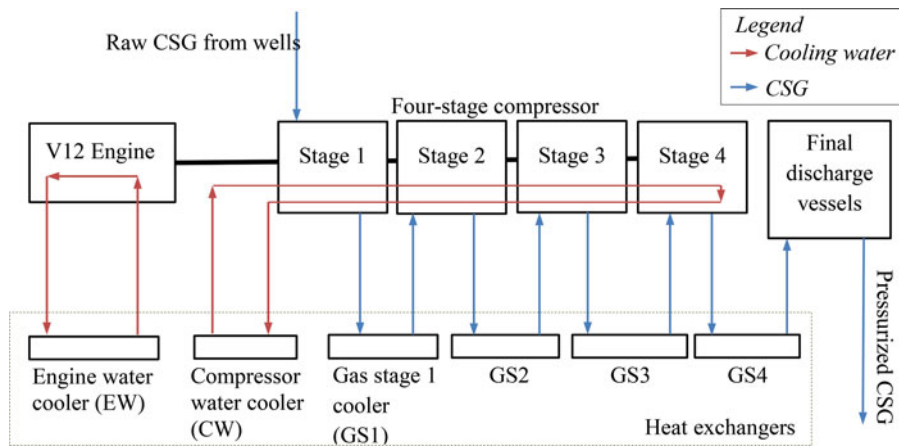
Figure 1. A brief sketch of the structure of the CSG compression unit.

water vapor in the raw gas can be removed and the dry CSG reaches a desired high pressure ready for pipe transport. The four-stage compressor is driven by a single internal combustion engine, and cooled is by cooling water through another heat exchanger named the compressor water cooler (CW). The internal combustion engine is fueled with CSG, and around 30% of its total combustion energy needs to be dumped by cooling water passing through the engine jacket. This loop of water is also cooled by a heat exchanger named the engine water cooler (EW).

Figure 1 shows a brief layout of the CSG compression unit.

The six heat exchangers (or cooler sections) are arranged horizontally on the top of the cooler unit shown in Figure 2. The cooler unit is equipped with two fans installed vertically at one end (denoted as Fan 1) and in the middle (denoted as Fan 2), respectively. Both the fans are also driven by the engine through one common long shaft, as seen in Figure 2b. The main dimensions and components of the cooler unit are indicated
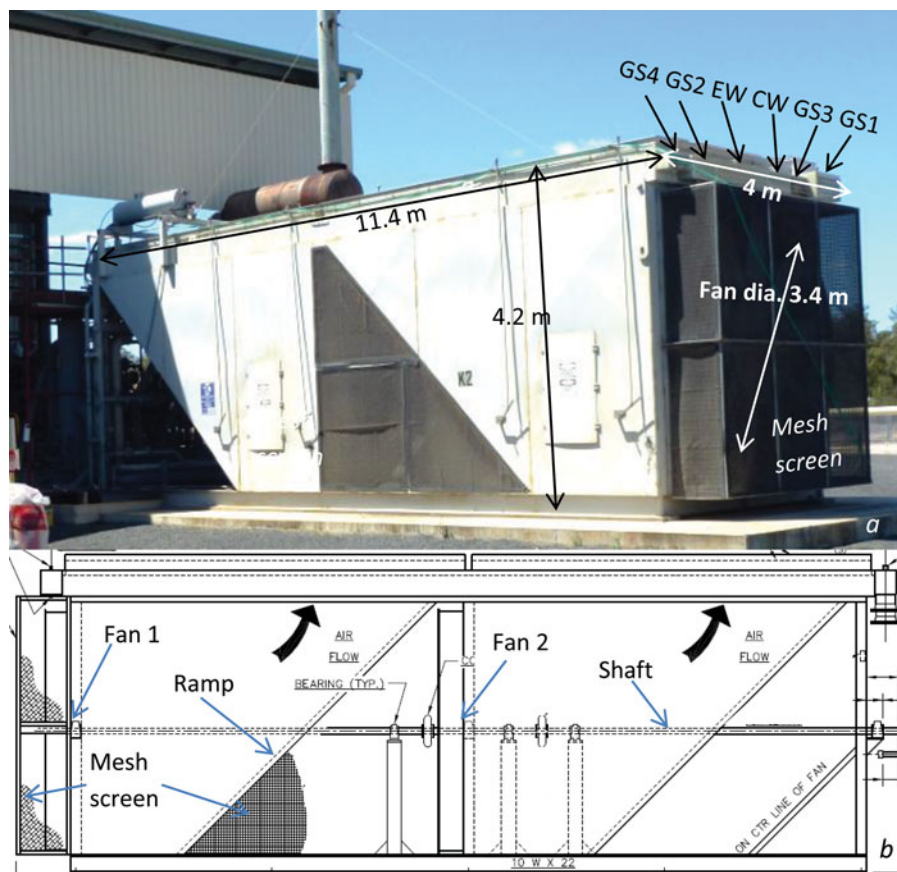

Figure 2. The six-section cooler unit (a) dimensions, (b) side view.

in Figure 2. All the cooler sections share the two fans but have independent liquid loops inside the tubes; therefore, their specifications are different except for the tube length.

In normal operations, the engine runs at a constant speed, and thus the fan speeds remain fixed. Ambient air is drawn into the cooler by the fans through the end and the two triangle inlets in the middle. Airflow inside the cooler is then lifted by the ramps and is distributed to the six cooler sections. As a type of cross-flow heat exchanger, the gas/water inside the cooler tubes flows horizontally. The design values provided by the manufacturer show that the two fans can deliver s total airflow rate of 154.36 kg/s, and all the cooler sections can adequately cool the tube-side gas or water even at 45°C ambient temperature. However, in real operations the engine encountered frequent automatic shutdowns in several recent summers, leading to unacceptable production reductions. It is known that the control system on the gas compression unit monitors the temperatures in the two cooling-water loops and four stages of gas cooling loops. Upper limits have been set in these temperatures— around 93°C for the cooling water and 180°C for the CSG, so that once any temperature reaches its limit the control system shuts down the engine immediately to avoid damages caused by overheating. It is highly suspected that the unexpected shutdowns are caused by this overheating protection mechanism. However, it was unknown which limit or limits were reached and the exact reasons.

In open literature reports, a wide range of topics is found in the area of fan-driven air-cooled finned-tube heat exchangers. Many of them focused on the cooling performance under different ambient conditions in different applications through experimental methods, such as references 3–7, and numerical modeling approaches, such as references 8–10. Some others studied the external influences on performances of mechanical cooler, such as plume recirculation and crosswinds [11–16]. Studies of the influence of fan blade angles on the cooling characteristics of the heat exchangers were also reported [17, 18]. Despite their large number, most studies were done for particular research purposes or industrial applications so that they provide little suggestion for the current cooling issue in the CSG compression facilities.

In this paper, a field instrument measurement on an operating cooler unit is reported, followed by an analysis using a one-dimensional (1D) analytical model and a three-dimensional (3D) computational fluid dynamics (CFD) model. By using different sensors, the air temperatures, speeds, and pressures, as well as the tube-side inlet/outlet temperatures on the cooler, have been measured. The experimental results are then used to validate both the 1D and the 3D models. After that, predictive simulations on the cooler performance under the summer peak condition are done by the models. The predictions are compared with the designed values, upon which final conclusions are drawn.

Field measurement

Measurement procedure

For air-side measurement, the air temperature and the speed were measured at the points 150 mm above each cooler outlet. The measurement points were arranged in an array of 6 × 9 throughout the plane, as shown in Figure 3a. Similarly, upwind of Fan 1 and Fan 2 inlets, a 4 × 5 array pattern and a triangle pattern of the speed and temperature measurement points were deployed 20 mm in front of the inlet mesh screens, respectively. Meanwhile, 13 air-speed sensors were mounted on two temporary diagonal beams, which were set at a distance of roughly 350 mm downstream of the fans, as indicated in Figure 3b. For pressure measurement, Pitot tubes were installed on both upstream and downstream of the screens and the fans in order to obtain the pressure differences across them. For tube-side measurement, one temperature sensor is installed each main inlet/outlet pipe. A summary of all the measurement points used on the cooler system is given in Table 1.

In order to minimize the number of necessary sensors, the arrays of measurement points outside the fan inlets and cooler exit were actually implemented by "scanning" the vertical pole and the top beam where the sensors were mounted on. The pole or beam stayed at one position for 15 minutes before it was moved to the next position, and the data were logged in each 15-min time window. Sensors in other locations kept continuous data logging throughout the experiment. A preliminary test on the cooler unit showed that over a period of 3 hours, the cooler performance was stable and multiple scan measurements at the fan inlets and cooler exit presented repeatable results. In this way, an acceptably accurate measurement can be accomplished at a relatively low cost of experiment.

Instrumentations

A data acquisition system (DAQ) was designed and set up to handle the aforementioned measurements. The system consists of a computer, sensors, analogue-to-digit modules, a weather station, and many other components. Figure 4 briefly illustrates the main components of the
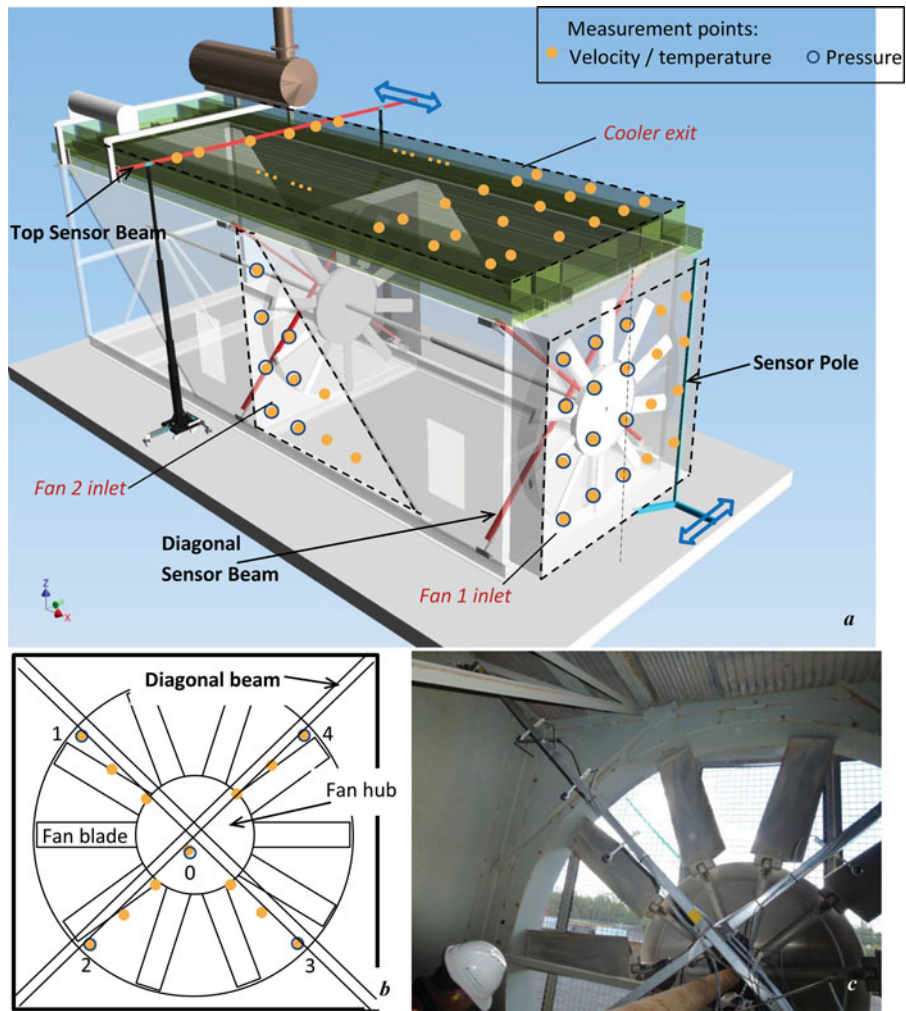
Figure 3. The measurement points outside the cooler unit (a) and on the diagonal beams inside the cooler (b) and (c). The numbers in (b) indicate the identification (ID) of pressure measurement points.
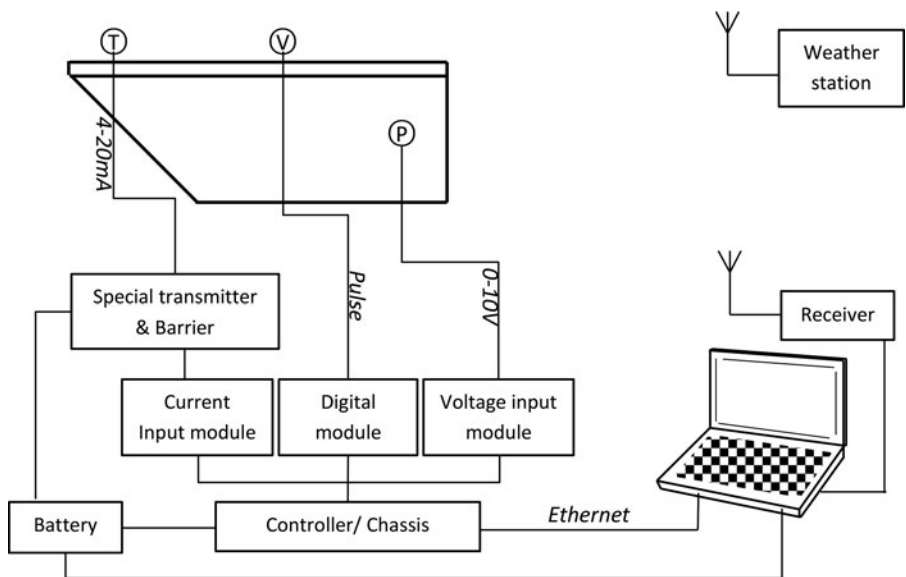

Figure 4. A sketch of the main components of the DAQ system.

Table 1. Summary of the measurement points on the cooler unit.

Parameters	Locations	Measurement points
Inlet air temperature	Screens (in front of)	20
Inlet air velocity	Screens (in front of)	20
Outlet air temperature	Above coolers	54
Outlet air velocity	Above coolers	54
Screen pressure drop	Screens (both sides of)	19 pairs
Fan pressure increase	Fans (both sides of)	5 pairs (for each fan)
Tube-side temperatures	Inside all 12 main pipes	1 (for each pipe)
Ambient temperature, pressure, wind speed, etc.	Away from the cooler unit	1

entire DAQ system, with Table 1 all the sensors listed in Table 2.

Modeling

1D analytical model

The current configuration of the cooler unit allows each of the six sections to dump heat from the tube-side liquid (i.e., the gas or the water) separately at a certain distributed airflow speed. In any cooler section, two balances have to be established in the heat transfer rate Q_{cs} and the air-side pressure drop ΔP_{cs}, which are expressed by Eqs. (1) and (2), respectively [19]:

$$Q_{cs} = m_a C_{pa} (T_{ao} - T_{ai})$$
$$= m_l C_{pl} (T_{li} - T_{lo}) = U_{cs} A_{cs} \Delta T_{lm} \quad (1)$$

$$\Delta P_{cs} = \frac{1}{2} K_{cs} \rho_a v_a^2 = K_{cs} \frac{m_a^2}{2\rho_a A_{fr}^2} \quad (2)$$

where subscripts a and l denote "air-side" and "liquid- or tube-side," respectively, and "cs" stands for cooler section.

In the heat transfer calculation, Eq. (1) involves the use of the arithmetic mean specific heat and the linear temperature difference for both the air and the tube sides. This use is valid as the specific heats of the CSG, the cooling water, and the air are all nearly linear in their own temperature and pressure ranges in this problem. U_{cs} is the heat transfer coefficient of the cooler section, which is given by [19, 20]

$$U_{cs} = \left[\frac{1}{e_f h_a} + \frac{A_a}{A_l h_l} + \frac{A_a ln\left(\frac{d_o}{d_i}\right)}{2\pi kL} + \left(\frac{A_a}{A_l} R_l + R_a\right) \right]^{-1} \quad (3)$$

where the term $(\frac{A_a}{A_l} R_l + R_a)$ represents the total thermal resistance due to the fouling on both sides of the tube walls. For convenience, the term can be denoted by a single parameter R_f, that is, $R_f = \frac{A_a}{A_l} R_l + R_a$.

The air-side heat transfer coefficients can be calculated using the empirical correlation [21]

$$Nu = \frac{h_{ae} d_r}{k} = 0.38 Re_c^{0.6} Pr^{0.333}$$
$$\times \left(\frac{\frac{(d_f^2 - d_r^2)}{2} + d_f t_{ft} + d_r (P_f - t_{ft})}{d_r P_f} \right)^{-0.15} \quad (4)$$

where the Reynolds number Re_c is based on the minimum flow area of the cooler section, and the effective coefficient $h_{ae} = e_f h_a$.

Inside the cooler tubes, the effective heat transfer coefficients for the water-based cooler sections are calculated by the correlation of Eq. (5) [19], while the ones for the gas-based sections apply the correlation of Eq. (6), which is valid for $0.6 < Pr_g < 0.9$ [20], namely,

$$Nu = \frac{h_i d_i}{k} = \frac{(f_D/8)(Re_w - 1000) Pr_w \left[1 + (d_i/L)^{0.67}\right]}{1 + 12.7(f_D/8)^{0.5} (Pr_w^{0.67} - 1)} \quad (5)$$

$$Nu = \frac{h_i d_i}{k} = 5 + 0.012 Re_g^{0.83} (Pr_g + 0.29) \quad (6)$$

where Re_w and Re_g are defined based on tube inner diameter d_i.

The thermal resistances caused by fouling are difficult to predict through a theoretical route. R_f is unknown for the current cooler sections and is estimated using the measurement data.

Table 2. List of sensors used in the field measurement on the cooler unit.

| Measuring parameter	Instrument type	Range	Accuracy
Air temperature	Thermocouple, 4—20 mA output	0—120	0.2°C
Tube-side temperature	Ex-rated RTD, 3 wire, 4—20 mA output	0—200	0.2°C
Air speed	Hot-wire anemometer	0—30 m/s	3% of reading
	Vane anemometers, voltage pulse output	0—15 m/s	0.1 m/s
Air pressure	Differential pressure transmitters, 0—10 V output	0—133.32Pa	0.25% of reading
	Differential pressure transmitters, 4—20 mA output	0—250 Pa	0.25% of FS or 0.5% of FS
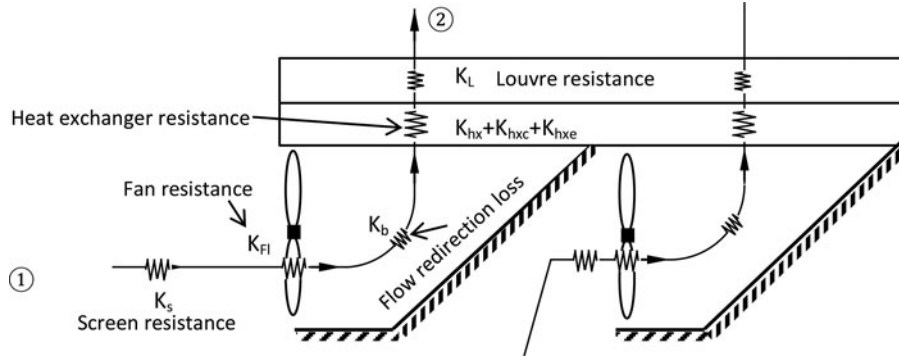
Figure 5. The schema of the pressure resistances in the airflow of the cooler unit.

For the pressure balance of any cooler section, K_{cs} in Eq. (2) is the pressure loss coefficient of the cooler section, and v_a is the mean air-face velocity based on the section's frontal area A_{fr}. K_{cs} is a function of the finned tube geometric parameters and the air speed as expressed in Eq. (7), which are all different in the six cooler sections:

$$Eu = \frac{K_{cs}}{2} = 18.93 n_r Re_c^{-0.316}$$

$$\times \left(\frac{P_t}{d_r}\right)^{-0.927} \left(\frac{P_t}{\sqrt{(P_t/2)^2 + P_l^2}}\right)^{0.515} + \frac{K_f}{2} \quad (7)$$

Here K_f is the additional resistance factor introduced considering the real conditions of the finned tubes, such as fouling and deformation of some fins.

As the cooler unit is essentially a multisection, mechanically driven heat exchanger system, the airflow through each section is distributed under the law that airflow naturally chooses the path with the smallest pressure resistance. The law results in a permanently stable state in the overall airflow such that the pressure drops for all six sections are the same, namely,

$$\Delta P_{cs1} = \Delta P_{cs2} = \cdots = \Delta P_{cs6} = \frac{1}{2} K_{hx} \rho_a \bar{v}_a^2 \quad (8)$$

Therefore, one can propose an overall mean air speed $\bar{v}_a$ and an overall mean pressure loss coefficient K_{hx} for the cooler unit. Considering the entire cooler system as a whole, there exists an equality between the pressure increased by the fans and the total loss along an air streamline throughout the system, as illustrated in Figure 5. The air pressure balance can be expressed as

$$P_1 - \left(P_2 + \alpha_{e2}\frac{1}{2}\rho_{a2}\bar{v}_a^2\right)$$

$$+ \left(\Delta P_{Fs} + \alpha_{eF}\frac{1}{2}\rho_{a1}v_{aF}^2\right) \approx \frac{1}{2}\sum^K \rho_a \bar{v}_a^2 \quad (9)$$

where ΔP_{Fs} is the static pressure increase provided by the fan. α_{e2} and α_{eF} are air speed correction factors.

In Eq. (9), the air face speed at the fans v_{aF} is related to the mean face speed at the cooler plane $\bar{v}_a$ as a result of the mass conservation. The total pressure loss coefficient $\sum K$ consists of the insect screen resistance K_s, the fan loss K_{Fl}, the loss due to the supporting structures and flow redirection K_b, the louver resistance K_L, and the heat exchanger bundle resistance (K_{hx}), including the losses due to the contraction K_{hxc} and the expansion K_{hxe}, that is,

$$\sum K = K_s + K_{Fl} + K_b + K_L + K_{hx} + K_{hxc} + K_{hxe} \quad (10)$$

Other pressure resistances are significantly smaller compared with the ones just described and therefore are not considered.

Equations (1) and (2) are solved by iterating the air mass flow rate m_a and the outlet temperatures (T_{ao} and T_{lo}) within their proper ranges. This iteration should be done for all the six cooler sections until all the m_a satisfy Eq. (8). Then the overall mean air speed $\bar{v}_a$ for the whole cooler unit is substituted into Eq. (9) to enable its equality. The calculation is implemented in MATLAB codes.

3D CFD model

Boundary conditions
A full-scale three-dimensional CFD model is set up based upon the cooler unit geometric dimension in Figure 6. The computational domain is a 60 m × 30 m × 20 m cuboid. The model only keeps the main features of the cooler realistic, while the detailed local structures that are less sensitive to the airflow are ignored.

The boundaries of the computational domain are indicated in Figure 6. Both pressure inlet and outlet boundaries apply zero pressure and zero pressure gradients, namely,

$$\begin{cases} P = 0 \\ \dfrac{\partial P}{\partial x_i} = 0 \\ T = T_{ab} \end{cases} \quad (11)$$
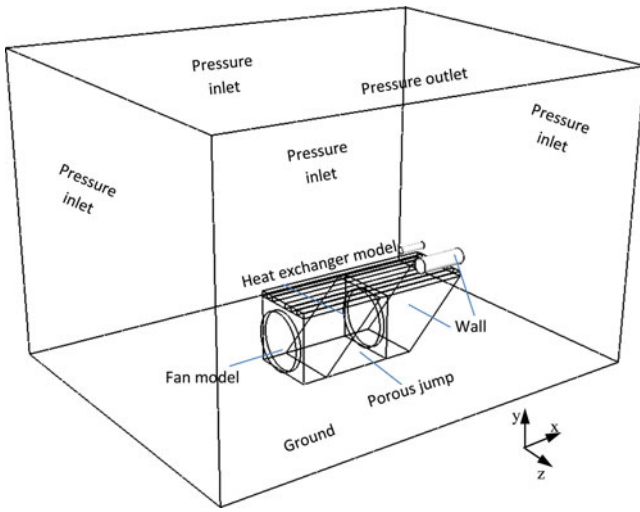
Figure 6. The CFD model of the cooler unit.

At the wall boundaries, the velocity and its gradients are specified as zero, and the temperatures are set to ambient. The insect screens in front of the fans are modeled by the porous jump boundary whose pressure drop is a function of normal air speed v_n at the face, that is,

$$\Delta P = av_n^2 + bv_n \tag{12}$$

where a and b are the coefficients.

Heat exchanger model

The six heat exchanger sections are simulated by a cell-based model consisting of six regular cuboid zones, each of which is discretized into structural cells—cubes, in a Cartesian system.
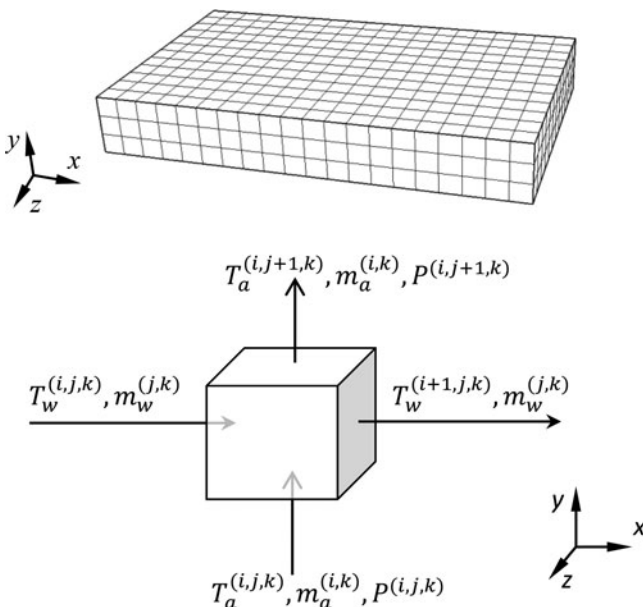

Figure 7. The cell-based heat exchanger model.

Figure 7 shows a cuboid model zone for one cooler section. The liquid flow direction aligns with the x-axis, while the airflow direction is along the y-axis. The quantities of either the tube side or the air side (temperature, mass flow rate, or pressure) within any cell (i, j, k) are transported along the streamlines. Therefore, the heat transfer in the cell has

$$
\begin{aligned}
Q^{(i,j,k)} &= m_w^{(j,k)} C_{pw}^{(j,k)} \left(T_w^{(i,j,k)} - T_w^{(i+1,j,k)} \right) \\
&= m_a^{(i,k)} C_{pa}^{(i,k)} \left(T_a^{(i,j+1,k)} - T_a^{(i,j,k)} \right) \\
&= U_a^{(i,j,k)} A^{(i,k)} \Delta T_{im}^{(i,j,k)}
\end{aligned} \tag{13}
$$

where the superscript of each variable represents for the sequence number of the cell. For the pressure calculation within the cell, this is followed by

$$\frac{P^{(i,j,k)} - P^{(i,j+1,k)}}{d^{(j)}} = \frac{1}{2\rho_a} \frac{K_{cs}}{t_{cs}} \left(\frac{m_a^{(i,k)}}{A^{(i,k)}} \right)^2 = S_{my}^{(i,k)} \tag{14}$$

where the pressure differnce is described in terms of a source term that is added into the corresponding momentum equation of the CFD model.

In the numerical computations, the CFD solver calculates the preceding two equations from the first cells at the boundaries to the last. Finally, the total heat transferred in the entire heat exchanger zone is available by adding the heats transferred in all the cells together, that is,

$$Q = \sum_{i,j,k} Q^{(i,j,k)} \tag{15}$$

while the overall pressure loss along an airflow path is given by Eq. (16):

$$\Delta P^{(i,k)} = \sum_j \Delta P^{(i,j,k)} = \frac{1}{2\rho_a} K_{cs} \left(\frac{m_a^{(i,k)}}{A^{(i,k)}} \right)^2 \tag{16}$$

Fan model

The fans in the cooler unit are modeled using a velocity-based model. The model treats the fan as a zero-thickness face with a specified profile of the air velocity normal to the fan face. The velocity is a function of the distance of the point from the fan center, r:

$$v = f(r) \tag{17}$$

The correlation is determined by the field measurement results.

Governing equations and solver

The airflow in the CFD models is assumed to be in a steady state and is governed by the conservation equations of mass, momentum, and energy. These conservation laws can be expressed by transport equations whose general
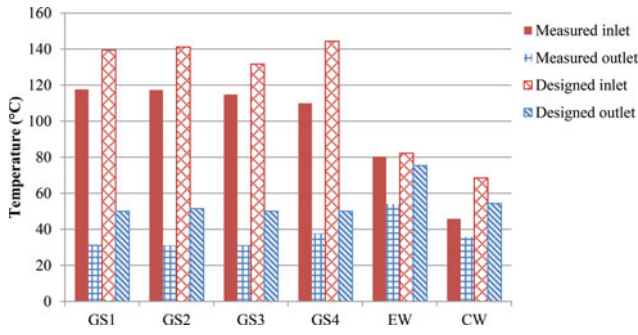
Figure 8. The measured tube-side inlet/outlet temperatures at $T_{ab} = 24.7°C$ with the designed values.

form is the following:

$$\nabla \left(\rho \vec{v} \phi \right) = \nabla \left(\Gamma_\phi \nabla \phi \right) + S_\phi \qquad (18)$$

with the generalized scalar ϕ, diffusion coefficient Γ_ϕ, and source term S_ϕ.

The source terms in the momentum equations refer to any additional resistances, such as pressure drops in the heat exchanger model, S_{my}. The energy source term in the energy governing equation represents the heat transferred with heat exchangers, calculated using Eq. (13). The turbulence model uses a two-equation Reynolds-averaged Navier–Stokes (RANS) model, SST k-ω. All numerical computations of the governing equations are run using the pressure-based steady-state solver with SIMPLE segregated algorithms and second-order upwind discretization.

Results and discussion

Cooling performance under the conditions on the test day

The field measurement results are presented next, followed by a comparison with the modeling outcomes. The mean ambient dry-bulb temperature during the measurement period was $T_{ab} = 24.7°C$ with mean wind speed less than 1 m/s.

The tube-side inlet/outlet temperatures are of the most importance among all the performance parameters of the cooler. The mean temperatures measured in the eight inlet/outlet pipes of gas-based cooler sections and four pipes of water-based cooler sections are shown in Figure 8, with comparisons against the design values provided by the manufacturer.

Although the design values are calculated based on a 45°C ambient temperature condition, the measured differences between the inlet and the outlet temperatures for all the gas-based cooler sections are generally close to those of the design. However, the temperature drop in the engine water cooler section (EW) in the measurement is
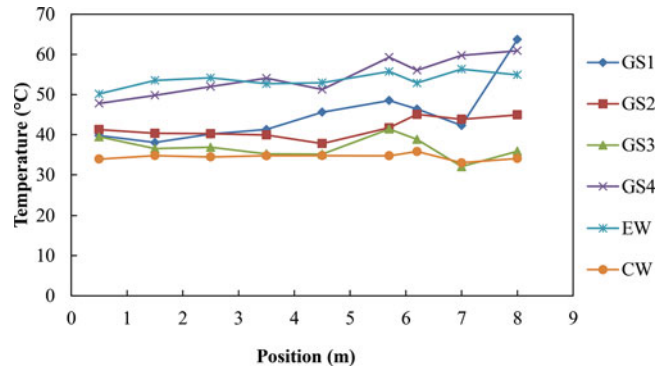

Figure 9. Air temperature above all the cooler sections at the nine measurement points at $T_{ab} = 24.7°C$, where *x*-axis indicates the measurement positions to Fan 1.

remarkably larger than its designed value. The reason of this was found to be that the actual cooling water flow rate was lower than that in the design, as the flow rate is adjustable.

The measurement results in the air side of the cooler are presented next. The measured mean air temperature and speed above the finned tubes along the cooler length are depicted in Figures 9 and 10, respectively, in which the horizontal axes represent the distances from measurement points to Fan 1. The exit air temperatures generally distribute more uniformly along the length of the cooler than the air speeds do. The considerable fluctuations in the air speeds along the cooler length at the sections except GS4 suggest that the actual airflow through the majority of the cooler face area is complex. Meanwhile, the air speed measured downstream of the fans with respect to the measurement position is plotted, as seen in Figure 11. The *x*-axis represents the distance of the measurement point to the fan centre along a radius of the fan. The speed data appears to be more scattered as the position gets closer to the fan hub. A power function with the exponent of 7.391 has been fitted to the data in Figure 11. It is clearly shown that the air speeds near fan blade tips are much higher.
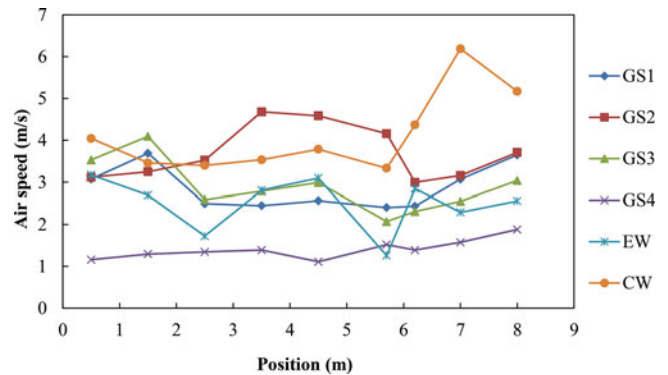

Figure 10. Air speeds above all the cooler sections at the nine measurement points, where *x*-axis indicates the positions to Fan 1.
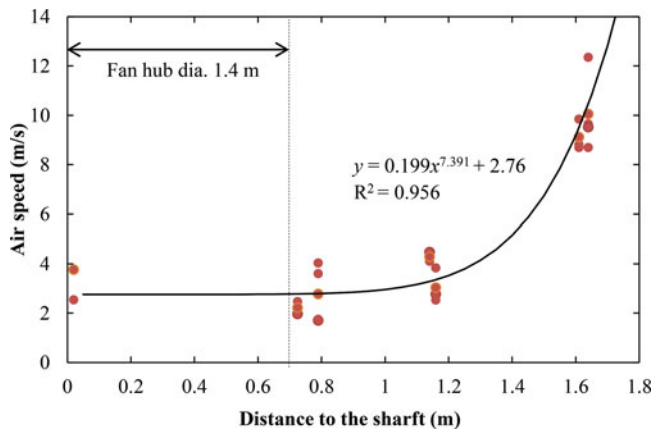
Figure 11. The air speeds downstream of the fans.

Figure 13. The temperature on the insect screen of Fan 1. The *x*-axis represents the height of the measurement point staring from the bottom edges of the screens.

The flow resistance across the insect screen is also of great interest as it directly influences the total air flow rate in the cooler. Figure 12 correlates the mean pressure drop and air speeds measured at the 12 measurement points on the insect screen of Fan 1 with the measurement height in meters. The mean values $\Delta P = 31.96$ and $\bar{v}_a = 3.25$ are obtained for the pressure drop and the air speeds, respectively. Then the pressure loss coefficient of the screen K_s is calculated using the both, $K_s = \frac{2\Delta P}{\rho_a \bar{v}_a^2} = 5.05$, where the ambient air density $\rho_a = 1.198$.

Similarly, the inlet air temperature at the Fan 1 insect screen with respect to the measurement height is plotted in Figure 13, with a comparison to the ambient temperature measured at the same heights away from the cooler unit. There is an increase in the inlet temperature in the upper part of the screen, which is explained using the CFD results in the following.

With the experimental results obtained in the field measurement, the thermal resistance factor R_f and the pressure loss factor K_f due to the fouling and other factors in the 1D analytical model were derived. R_f was calculated by applying Eqs. (1) and (2) where all the temperature
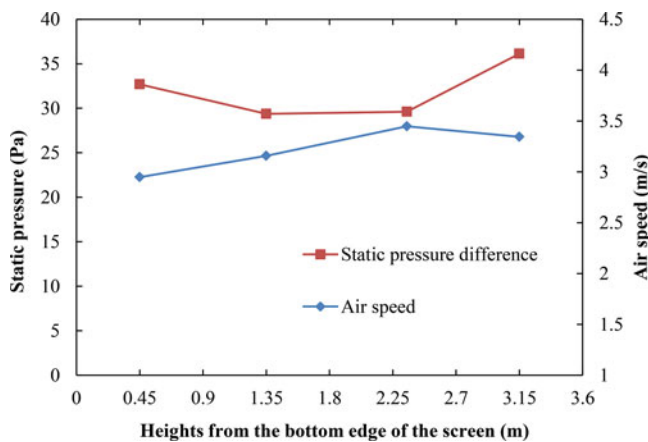
differences and the air-side mass flow rate for each cooler section were known from the measurement. The derivation of K_f used an iterative way that adjusted the K_f for each cooler section while keeping the total air mass flow rate of the cooler the same as the measured one, until all the six air mass flow rates matched the ones derived from the measurement. For the 3D CFD model, the measured inlet temperature in each cooler section, the air speed at the fan, and the ambient conditions were applied in the boundaries. In this way, both the 1D and 3D models are able to repeat the cooler performance under the test condition.

The airflow field under the test condition is visualized using vectors extracted from the CFD results. Figures 14a and 14b are the plane velocity vectors in the mid-*xy* plane and mid-*xz* plane, respectively. The airflow field inside the cooler unit appears rather complicated. In Figure 14a, the four major horizontally spinning vortices near the side walls downstream to the two fans are due to the contraction–expansion effect of the airflow when it flows through the fans. The vortices after Fan 2 are larger than the two after Fan 1, which cause more airflow to concentrate in the middle axis of the cooler. The complexity of the flow field is reflected by the air speed distribution at the outlet of the heat exchangers which is shown in Figure 10. It is noted in Figure 14b that there is a clear vertex at the upper left corner of the cooler unit. The hot air in the zone recirculates into the chamber after it leaves the cooler sections, because of the strong suction force of the fan near its edge.

The air temperature at the outlet of the six cooler sections is demonstrated through the contours in Figure 15. As indicated in the figure, the two passes of the tube-side fluid in a cooler section are arranged at the plane perpendicular to the airflow. Therefore, the highest outlet air temperature occurs near the entry of the first pass in each cooler section; along the tube-side flow route, the air temperature gradually decreases. The contours show that

Figure 12. The pressure drop and the air speed measured on the insect screen of Fan 1. The *x*-axis represents the height of the measurement point staring from the bottom edges of the screens.
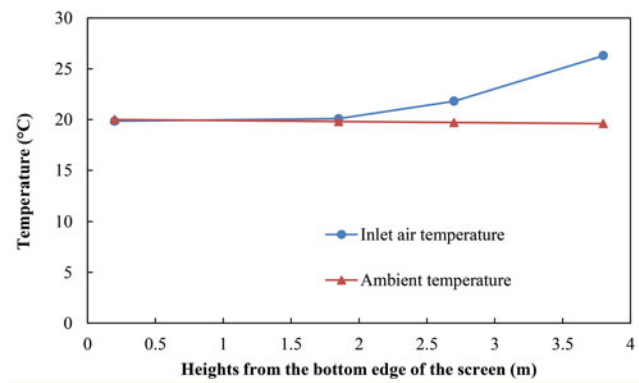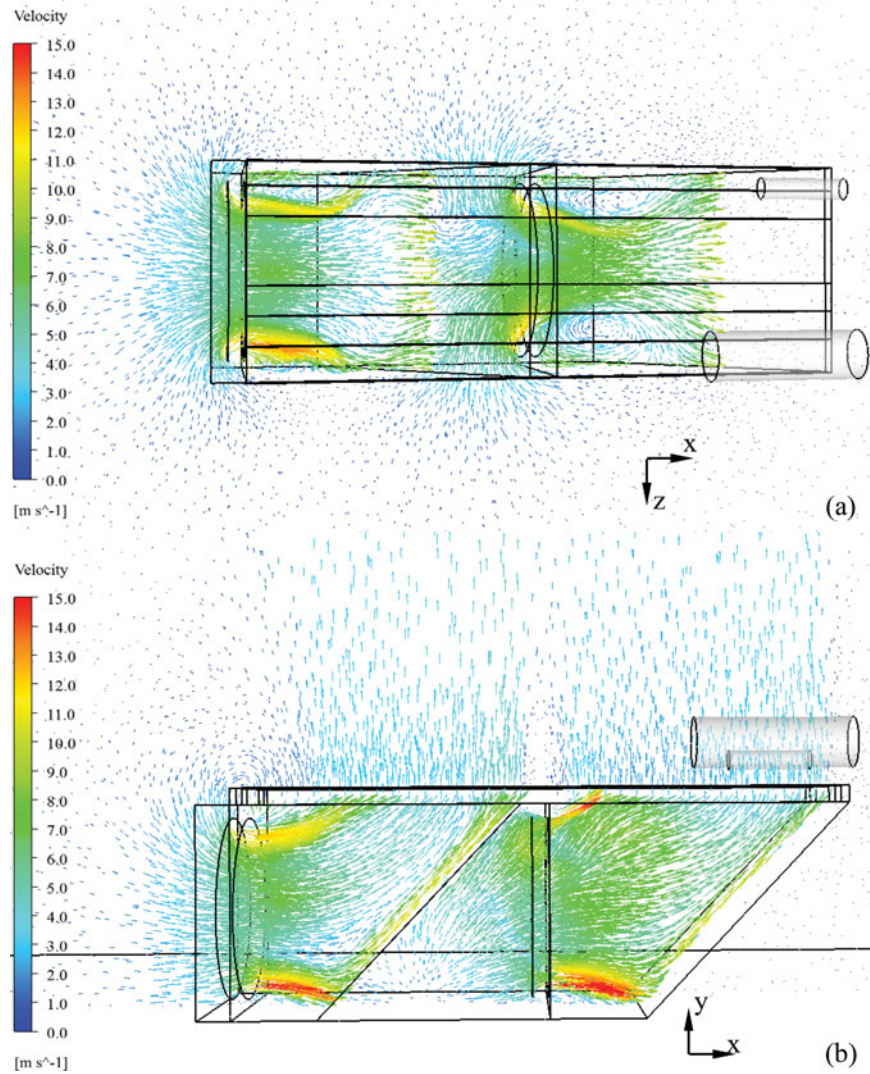
Figure 14. The plane velocity vectors at middle horizontal plane (a) and middle vertical plane (b) in cooler unit under the design condition.
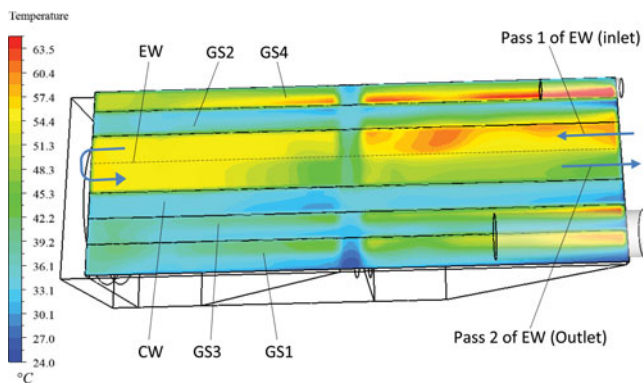
Figure 15. Air temperature contours at the outlet plane of the cooler unit under the condition on the test day.

Figure 16. The air outlet temperatures of GS4 and EW obtained in the CFD model are compared with the measured result.

the outlet air temperature of the cooler unit varies in the range of 30°C to 65°C.

Quantitatively, the outlet air temperatures at EW and GS4 extracted from the CFD results are compared with the measured ones in Figure 16. Here the x-axes represent the horizontal distances of the measurement points to Fan 1. A satisfactory agreement between both the results is achieved.

Figure 17. Air temperature contours at the mid-*xy* ($z = 0$) of the cooler unit under the real condition.

Figure 17 plots the air temperature contours at the mid-vertical plane of the cooler unit. The aforementioned air recirculation in the upper part of Fan 1 is verified by the air temperature distribution, and the hot air even reaches more than half the length of the first cooler chamber. The observation explains the reason for the increase in the measure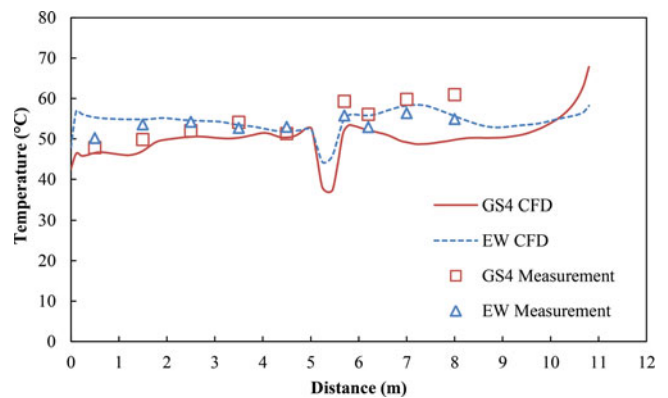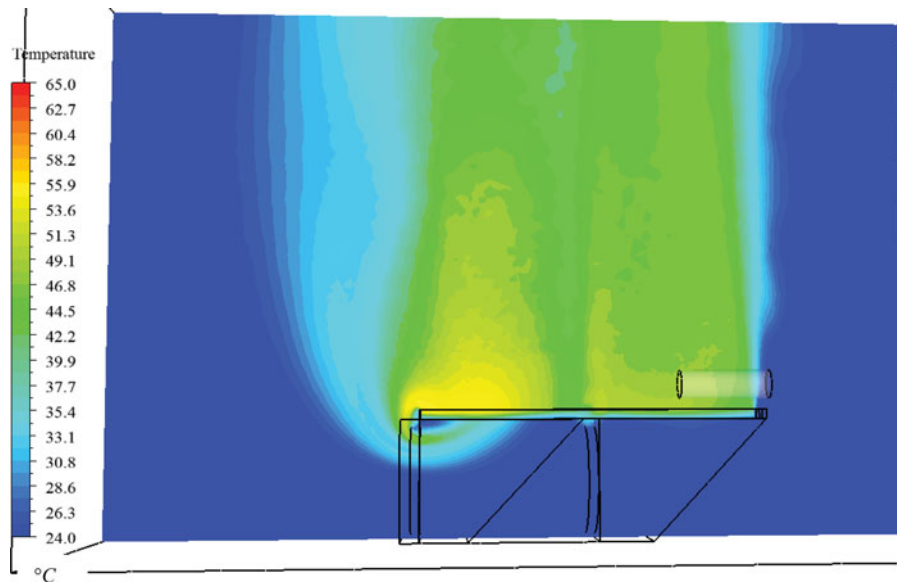d inlet air temperature at Fan 1 insect screen in Figure 13. The air recirculated into the region underneath the finned tubes is almost 10°C warmer than the ambient air, which could reduce the overall heat rejection capacity of the cooler sections.

Overall, the simulated results in both the 1D and the 3D numerical models are summarized in Tables 3 and 4, with comparisons to the derived values from the field measurement. Differences between any two results are all less than 10%, which indicates that the modeling can repeat what was measured in the field test in a considerably accurate way.

Performance predictions under summer peak condition

Now with the validated 1D analytical and the 3D CFD models, the cooling performance of the cooler unit can be simulated under the summer peak condition, which presumes the ambient dry-bulb temperature to be 45°C and no wind to exist. As the inlet air is much warmer in this case, the heat transfer efficiency must change, and so do the other thermal properties at either the air side or tube side. To establish the balance in the heat transfer equations, the following assumptions are made:

Table 3. Modeling results and field measurement for the key tube-side parameters.

		GS1	GS2	GS3	GS4	EW	CW
tube outlet temperature (°C)	Measurement	31.44	31.07	31.2	37.64	53.95	35.65
	1D model	31.66	30.56	31.1	38.37	54.38	34.56
	3D model	31.53	30.99	30.62	39.25	54.02	34.43
Heat transferred (kW)	Measurement	327.69	323.61	308.2	234.79	1179	176.7
	1D model	327.7	333.3	315.5	250.90	1165	188.8
	3D model	319.5	327.04	311.5	253.4	1183.4	178.9

Table 4. Modeling results and field measurement for the key air-side parameters.

		GS1	GS2	GS3	GS4	EW	CW
Air outlet temperature (°C)	Measurement	43.32	41.67	37.72	54.55	53.71	34.47
	1D model	39.49	39.64	37.73	54.32	52.37	32.64
	3D model	39.12	38.18	38.32	53.11	52.31	33.13
Air face velocity (m/s)	Measurement	2.77	3.69	3.18	1.41	2.5	3.7
	1D model	2.76	3.58	3.17	1.54	2.46	3.52
	3D model	2.64	3.53	3.0	1.52	2.56	3.72

Table 5. Performance prediction of the cooler unit under the high-temperature condition.

Parameter	1D prediction	3D prediction	Design value	Difference
Mean inlet air temperature,°C	45	45	45	—
Total air mass flow rate (kg/s)	128.37	130.7	154.36	− 16.1%
GS1 (at designed flow rate 1.59 kg/s, total heat rejected 339.5 kW)				
Mean air face velocity, m/s	2.76	2.85	2.98	− 5.9%
Air outlet temperature,°C	61.34	58.5	N/A	N/A
Tube-side inlet temperature,°C	139.3	141.2	139.4	0.6%
Tube-side outlet temperature,°C	52.57	54.2	50	6.8%
Effective heat transfer coefficient, W/(m²-K)	252.9	247.24	259.5	− 3.6%
GS2 (at designed flow rate 1.58 kg/s, total heat rejected 342.3 kW)				
Mean air face velocity, m/s	3.5	3.48	3.29	6.1%
Air outlet temperature,°C	61.37	63.56	N/A	N/A
Tube-side inlet temperature,°C	138.4	142.68	141.1	− 0.4%
Tube-side outlet temperature,°C	51.33	53.25	51.4	1.7%
Effective heat transfer coefficient, W/(m²-K)	401.9	401.16	396.3	1.3%
GS3 (at designed flow rate 1.50 kg/s, total heat rejected 311.9 kW)				
Mean air face velocity, m/s	3.2	3.26	3.7	− 12.7%
Air outlet temperature,°C	62.87	61.2	N/A	N/A
Tube-side inlet temperature,°C	137.02	137	131.67	4.1%
Tube-side outlet temperature,°C	56.04	55.69	50	11.7%
Effective heat transfer coefficient, W/(m²-K)	389	379.889	507.1	− 24.2%
GS4 (at designed flow rate 1.36 kg/s, total heat rejected 355 kW)				
Mean air face velocity, m/s	1.74	1.78	4.1	− 57.1%
Air outlet temperature,°C	78.4	74.39	N/A	N/A
Tube-side inlet temperature,°C	156.8	155.3	144.4	8.1%
Tube-side outlet temperature,°C	64.1	68.37	50	32.5%
Effective heat transfer coefficient, W/(m²-K)	449.3	459.63	566.1	− 19.7%
EW (at designed flow rate 28.67kg/s, total heat rejected 1312.7 kW)				
Mean air face velocity, m/s	2.48	2.56	3.21	− 21.5%
Air outlet temperature,°C	78.2	77.56	N/A	N/A
Tube-side inlet temperature,°C	97.1	97.9	82.2	18.6%
Tube-side outlet temperature,°C	84.57	86.11	75.4	13.2%
Effective heat transfer coefficient, W/(m²-K)	651.3	649.19	787.9	− 17.6%
CW (@designed flow rate 5.03 kg/s, total heat rejected 296.5 kW)				
Mean air face velocity, m/s	3.51	3.64	4.13	− 13.4%
Air outlet temperature,°C	57.91	59.25	N/A	N/A
Tube-side inlet temperature,°C	76.3	78.9	68.4	13.5%
Tube-side outlet temperature,°C	59.5	62.7	54.4	12.3%
Effective heat transfer coefficient, W/(m²-K)	574.0	562.9	729.0	− 22.0%

1. At the peak of a summer day, the total redundant heat that needs to be dumped by each cooler section is the greater value between the designed one and measured one.
2. The tube-side flow rates (i.e., the CSG and the water flow rates) are the same as the designed values.
3. The fan remains able to deliver a constant mass of airflow per second.

Assumption 1 is based on the ideology that whichever is larger between the designed value and measured one should be considered closer to the real heat load under the summer peak condition.

The prediction results of the 1D and the 3D models are quantitatively shown in Table 5, with a comparison against the design values under the same condition. The "Difference" in Table 5 is defined as

$$Difference = \frac{X_{prediction} - X_{design}}{X_{design}} \times 100\% \qquad (19)$$

where $X_{prediction}$ and X_{design} are the mean value of the two model prediction results and the measured value for any parameter in the table.

The quantitative comparison shows that the modeling prediction result diverges from change trends of the cooling performances among the six cooler sections. In GS1 and GS2 cooler sections, the predicted cooling performance is quite close to the design values. The other cooler sections, on the other hand, are predicted to perform worse than what they were designed to be, such as for the GS4 cooler section, whose air face velocity and effective heat transfer coefficient are both significantly lower.

The most critical cooling performance degradation is in the EW cooler section. The water inlet temperature for the heat exchanger of 97.1°C is actually the temperature leaving the engine jacket. And this temperature is already higher than its upper limit, which can trigger the protective engine shutdown, as mentioned in the introduction.
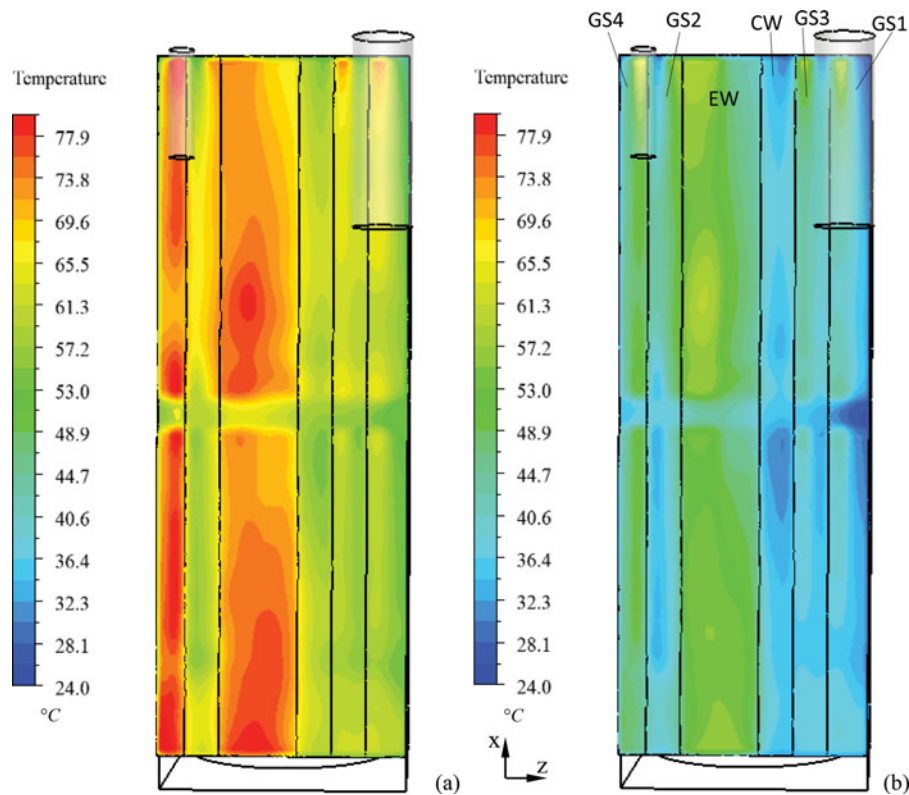
Figure 18. The comparisons of temperature distributions above the cooler under (a) the summer peak condition and (b) the real condition on the test day.

This happens because the water leaving the cooler is not sufficiently cooled down to a proper temperature, which is supposed to be around 75.4°C. Once it is heated by the hot engine again the temperature is able to exceed the limit. It is found that the poor cooling performance is caused by the large reductions in the air speed and the total effective heat transfer coefficient, which account for 21.5% and 17.6% of their designed values, respectively. The former is a direct result of less efficiency of the fans and/or more resistances occurring in the airflow; the latter is because of the fouling on the finned-tube surfaces. With these two adverse factors, the water in the cooler section cannot be sufficiently cooled down under the peak summer condition, leading to an over-limit engine-exit water temperature.

A qualitative comparison of the outlet air temperature contours of the six cooler sections is made between the peak summer condition case and the field measurement condition case in Figure 18. The temperature distributes in a similar pattern between both the cases; however, the overall temperature in the former is much higher. High temperature appears mainly in the EW and GS4 cooler sections.

It should be noted that the preceding prediction results are based on the "fixed total heat load"

assumption. However, in reality the engine consumes more fuel, because the compression work for the CSG at a higher temperature is even harder. As the result, the extra heat dumped by the engine cooling water is actually more than the one assumed in the preceding. This will lead to an even higher water temperature leaving the engine jacket. Therefore, the prediction presented here is still conservative.

Conclusions

A practical cooling issue in the productions of coal seam gas is investigated in this study. The CSG gas compression units suffer frequent automatic shutdown during operations on summer days, which is out of the expectations of the manufacturer's design. The study uses both the 1D analytical and the 3D CFD models to predict the cooling performance of the cooler unit under the summer peak condition. These models were validated by the field instrument measurement on one of the operating CSG gas compression facilities.

The modeling prediction suggests that the cooling performances of two gas-stage cooler sections (GS3 and GS4) and two water cooler sections (EW and CW) are generally

worse than their designed values at 45°C ambient temperature. Among the four, the EW cooler section is of the most critical consequence to the entire CSG compression facility. The cooling water in the EW cooler section is not adequately cooled; thus, when the water reenters the engine jacket, it is easy to reach a temperature that is already higher than 93°C—the maximum allowable cooling water temperature. In the circumstances, the control system terminates the engine operation immediately to prevent the engine from being too hot. The poor cooling in the cooler unit is caused by the significant reductions in two key parameters. One is the airflow rate, which is a direct result of less efficiency of the fans and/or more resistances in the airflow. The other one is the total effective heat transfer coefficient of the heat exchanger bundles, which is affected by the fouling on both the air-side and the tube-side surfaces. Therefore, the study would suggest these methods to improve the cooler performance: (1) Enlarge the airflow rate, (2) minimize the flow resistances in the cooler unit, and (3) remove the fouling on the heat exchangers.

Nomenclature

A	area (m²)
a	constant
A_a, A_{fr}, A_f	air-side area, frontal area, and fin-root area, respectively (m²)
A_c	surface area of numerical cell (m²)
b	constant
C_p	specific heat (J kg⁻¹ K⁻¹)
CW	compressor water cooler
CFD	computational fluid dynamics
CSG	coal seam gas
DAQ	data acquisition system
d_o, d_i	tube outside and inside diameter (m)
d_f, d_r	fin diameter, tube root diameter (m)
Eu	Euler number
EW	engine water cooler
e_f	fin surface effectiveness
f_D	tube friction coefficient
GS	gas stage cooler
H	height, elevation (m)
h	convective heat transfer coefficient (W m⁻² K⁻¹)
K	pressure loss coefficient
$K_s, K_{Fl}, K_b, K_L, K_{hx}, K_{hxc}, K_{hxe}$	pressure loss coefficient due to insect screen, fan, supporting structures and flow redirection, louver, heat exchanger bundle resistance, heat exchanger contraction effect, and heat exchanger expansion effect
k	thermal conductivity (W m⁻¹ K⁻¹)
L	tube length (m)
m	mass flow rate (kg/s)
Nu	Nusselt number
n_r	number of tube rows in a heat exchanger bundle
P	pressure (Pa)
ΔP_{FS}	fan static pressure difference (Pa)
Pr	Prandtl number
p_f	fin pitch (m)
p_l, p_t, p_d	tube transversal, longitudinal, and diagonal pitch, respectively (m)
Q	heat transfer rate (W)
R	thermal resistance (m² K W⁻¹)
R_f	thermal resistance due to fouling (m² K W⁻¹)
Re	Reynolds number
Re_c	Reynolds number based on minimum flow area
r	distance to fan center (m)
S_{my}	source term in pressure governing equation (Pa)
S_ϕ	volumetric source term for variable quantity ϕ
T, T_{ab}	temperature, ambient temperature (K)
t_{ft}	fin tip thickness (m)
ΔT_{lm}	logarithmic mean temperature difference (K)
U	overall heat transfer coefficient (W m⁻² K⁻¹)
V_c	numerical cell volume (m³)
$\vec{v}$	velocity vector
v_a	air velocity scalar (m s⁻¹)

$\bar{v}_a$ — mean air velocity (m s^{-1})

v_{aF} — air speed at fans (m s^{-1})

v_n — air velocity normal to a face (m s^{-1})

X — a symbol for an arbitrary quantity calculated

x, y, z — Cartesian coordinates

Greek symbols

α_{e2}, α_{eF} — air speed correction factors

Γ_ϕ — diffusion coefficient for variable quantity ϕ

$\rho_a, \bar{\rho}$ — air density and mean density (kg m^{-3})

ϕ — scalar quantity ($u, v, w, T, k, \varepsilon$ …)

ω — turbulence energy specific dissipation rate (s^{-1})

Subscripts

a, l — air side, liquid (tube) side

cs — cooler section

e — effective

f — fin or fouling

g — coal seam gas

hx — heat exchanger

i, o — inside or inlet, outside or outlet

w — water

Notes on contributors

Yuanshen Lu has been a research fellow at the School of Mechanical and Mining Engineering of the University of Queensland since he received his Ph.D. degree from the university in 2015. He obtained his master's and bachelor's degrees in Central South University, China. He has more than 5 years of research experience in natural draft cooling towers and heat exchangers. His current interests are in advanced technologies in small natural draft hybrid cooling towers, ground source heat pumps, and heliostat maintenance methodologies for concentrated solar power plants.

Zhiqiang Guan is a senior research fellow at the School of Mechanical and Mining Engineering of the University of Queensland, Australia, and has many years of industry experience in mining equipment and structure design, dynamic modeling, conditional monitoring, and reliability analysis. His current research interests include natural draft cooling systems design and analysis for solar thermal power plants, CFD modeling, heat exchanger design, hybrid cooling research, and solar mirror cleaning.

Kamel Hooman completed his Ph.D. at the University of Queensland. He is a T&R academic staff member within the School of Mechanical and Mining Engineering. His research interests are in thermofluids and energy. He is the Director of QGECE (Queensland Geothermal Energy Centre of Excellence) and has a strong research record in the field of heat transfer and energy. He is recognized worldwide for his work on heat exchangers, which are essential technology for power generation and energy management. He has pioneered the use of metal foams in fuel cells, supercritical heat exchangers for geo/solar thermal power plants, and scaling of natural draft dry cooling towers.

Prashant S. Parulekar has more than 24 years of international experience in the system design, construction and operation of large-scale energy projects and facilities. He has a master's degree in mechanical engineering (M.Phil.) from the University of Queensland and a bachelor's degree from the University of Poona, India. He is currently the Technical Authority (TA2) for Rotating Machinery at Arrow Energy and provides technical advice to greenfield and brownfield projects, besides ongoing plant operations.

ORCID

Kamel Hooman http://orcid.org/0000-0003-0282-7960

References

[1] Shah, R. K., and Sekulić, D. P., *Fundamentals of Heat Exchanger Design*, John Wiley & Sons, Hoboken, NJ, 2003.

[2] Department of Natural Resources and Mines, *Queensland's Coal Seam Gas Overview*, Queensland Government report, Queensland, Australia, February 2013.

[3] Shklover, G. G., Heat Transfer in Condensation of Steam on Finely-Finned Horizontal Tubes, *Heat Transfer Soviet Research*, vol. 13, pp. 108–114, 1981.

[4] Chen, L., Experimental Investigation of Plastic Finned-Tube Heat Exchangers, With Emphasis on Material Thermal Conductivity, *Experimental Thermal and Fluid Science*, vol. 33, pp. 922–928, 2009.

[5] Guo, Y., Ventilation and Air Conditioning Experimental Study of Heat Transfer and Resistance on Finned Tube Exchanger, *Proceedings of the 8th International Symposium on Heating, Ventilation and Air Conditioning: HVAC&R Component and Energy System*, vol. 2, pp. 645–652, 2014.

[6] Jang, J.Y., Experimental and 3-D Numerical Analysis of the Thermal-Hydraulic Characteristics of Elliptic Finned-Tube Heat Exchangers, *Heat Transfer Engineering*, vol. 19, pp. 55–67, 1998.

[7] Aganda, A. A., A Comparison of the Predicted and Experimental Heat Transfer Performance of a Finned Tube Evaporator, *Applied Thermal Engineering*, vol. 20, pp. 499–513, 2000.

[8] He, W. F., Performance Prediction of an Air-Cooled Steam Condenser Using UDF Method, *Applied Thermal Engineering*, vol. 50, pp. 1339–1350, 2013.

[9] Torikoshi, K., and Xi, G., A Numerical Study of Flow and Thermal Fields in Finned Tube Heat Exchangers (Effect Of The Tube Diameter), *Proc. ASME Heat Transfer Division*, San Francisco, CA, vol. 317, no. 1, pp. 453–458, 1995.

[10] Yang, L., Numerical Study on Flow and Heat Transfer Characteristics of Finned Tube Bundles for Air-Cooled Heat Exchangers of Indirect Dry Cooling Systems in Power Plants, *Zhongguo Dianji Gongcheng Xuebao*, vol. 32, pp. 50–57, 2012.

[11] Kroger, D. G., Reduction in Performance Due to Recirculation in Mechanical Draft Cooling Towers, *Heat Transfer Engineering*, vol. 10, pp. 37–43, 1989.

[12] Duvenhage, K., and Kroger, D. G., Plume Recirculation in Mechanical-Draft Air-Cooled Heat Exchangers, *Heat Transfer Engineering*, vol. 16, pp. 42–49, 1995.

[13] Duvenhage, K., and Kroger, D. G., The Influence of Wind on the Performance of Forced Draught Air-Cooled Heat Exchangers, *Journal of Wind Engineering and Industrial Aerodynamics*, vol. 62, pp. 259–277, 1996.

[14] Cooper, J. W., , Recirculation and Interference Characteristics of Circular Mechanical Draft Cooling Towers, *Journal of the Cooling Tower Institute*, vol. 6, no. 1, pp. 28–35, 1985.

[15] Bender, T. J., Bergstrom, D. J., and Rezkallah, K. S., A Study on the Effects of Wind on the Air Intake Flow Rate of a Cooling Tower: Part 2. Wind Wall Study, *Journal of Wind Engineering and Industrial Aerodynamics*, vol. 64, pp. 61–72, 1996.

[16] Bender, T. J., Bergstrom, D. J., Rezkallah, K. S., A Study on the Effects of Wind on the Air Intake Flow Rate of A Cooling Tower: Part 3. Numerical Study, *Journal of Wind Engineering and Industrial Aerodynamics*, vol. 64, pp. 73–88, 1996.

[17] He, W., Influence From the Blade Installation Angle of the Windward Axial Fans on the Performance of An Air-Cooled Power Plant, *Energy*, vol. 60, pp. 416—425, 2013.

[18] Nelson, J. E., and Phalen, T. E., , *Influence of Condenser Fan Blade Pitch on Steam Turbine Performance at the Norton P. Potter II Station*, American Society of Mechanical Engineers, New York, NY, pp. 1–5, 1992.

[19] Kroger, D. G., *Air-Cooled Heat Exchangers and Cooling Towers*, vol. 2, pp. 38–50, Pennwell Corp, Tulsa, OK, 2004.

[20] Sadic Kakac, H. L., *Heat Exchangers Selection, Ratting, and Thermal Design*, 2nd ed., CRC Press, New York, NY, 2002.

[21] Ganguli, A., and Tung, S. S., and Arametric, T. J, Study of Air-Cooled Heat Exchanger Finned Tube Geometry, *American Institude of Chemical Engineers Symposium Series*, vol. 81, pp. 122–128, 1985.